Neuroimage: Reports 1 (2021) 100051

Contents lists available at ScienceDirect

Neuroimage: Reports

journal homepage: www.sciencedirect.com/journal/neuroimage-reports

The impact of gliomas on resting-state oscillatory activity and connectivity: A magnetoencephalography study

Fatemeh Shekoohishooli [a,1], Federico Chella [a,1], Massimo Caulo [a,b], Riccardo Navarra [a], Matteo Rapino [a], Vittorio Pizzella [a,b], Laura Marzetti [a,b,*]

[a] Department of Neuroscience, Imaging and Clinical Sciences, "G. d'Annunzio University" of Chieti-Pescara, 66100, Chieti, Italy
[b] Institute for Advanced Biomedical Technologies, "G. d'Annunzio University" of Chieti-Pescara, 66100, Chieti, Italy

ARTICLE INFO

Keywords:
Glioma patients
Resting-state
Magnetoencephalography
Functional connectivity

ABSTRACT

Gliomas disturb brain functions, contributing to abnormal neuronal activity and connectivity changes that can be effectively investigated using magnetoencephalography (MEG). In this work, we used MEG to evaluate frequency-specific alterations of brain activity and functional connectivity in glioma patients. Two consecutive 5-min sessions of eyes-closed resting-state brain activity were recorded from ten glioma patients and ten age-matched healthy subjects. Modulations of power and functional connectivity, within the patient group and between patients and the healthy control group, were assessed in terms of the Neural Activity Index and the Multivariate Interaction Measure, respectively. These quantities were calculated in individualized frequency bands (delta, theta, lower alpha, upper alpha and beta) to account for changes in spectral peaks in patients.

We report a decrease in power in tumor and peri-tumor regions in the upper-alpha and beta bands with respect to the rest of the brain, paired to a decrease in lower and upper-alpha band functional connectivity of the tumor and peri-tumor regions. In comparison with healthy subjects, we observe a global enhancement in power in lower-alpha in patients.

Overall, our study shows that glioma infiltration can widely influence brain local and long-range synchrony in an individualized frequency-specific manner.

1. Introduction

Gliomas alter brain electromagnetic signals, indexing abnormal neuronal activity and connectivity changes that can be effectively investigated using non-invasive electrophysiological techniques, such as Electroencephalography (EEG) and magnetoencephalography (MEG). In particular, MEG reflects the intracellular electric current flow in the brain and is thus able to provide direct information of neural activity by non-invasively recording the magnetic fields (Baillet, 2017). This technique has unique profits, such as its safeness, a temporal resolution better than 1 ms and a reasonable spatial resolution (in the order of millimeters) (Hämäläinen et al., 1993; Pizzella et al., 2014).

To date, MEG signals have been used to assess abnormal brain functions under various pathological conditions (for reviews see Hari et al., 2018; Bagić et al., 2020). In the framework of brain tumors, studies have shown that patients demonstrate pathological slow waves in MEG recordings, indicating an alteration in local synchronization processes in specific brain areas (e.g., Vieth et al., 1996; De Jongh et al., 2003; Baayen et al., 2003; Butz et al., 2004; Bartolomei et al., 2006a; Bosma et al., 2008a,b). MEG is also an excellent tool for the investigation of long-range brain synchronization (Marzetti et al., 2019) measured by functional connectivity during task execution and in the absence of an externally cued task, i.e., in the so-called 'resting-state'. The mapping of functional connectivity and brain networks in the resting-state has a long-lasting tradition in MEG (Stam et al., 2006; Schnitzler and Gross, 2005; Brookes et al., 2011; de Pasquale et al., 2012; Hillebrand et al., 2012; Marzetti et al., 2013). MEG resting-state functional connectivity analysis has characterized not only the level of co-activation between brain regions but also the phase coupling of their respective oscillatory signals (Engel et al., 2013), a measure of interaction between brain regions sharing the same excitability state (Fries, 2005).

Among the different metrics based on phase synchronization of oscillatory signals, the Multivariate Interaction Measure (MIM) (Ewald et al., 2011) detects functional connectivity between multivariate time

* Corresponding author. Institute for Advanced Biomedical Technologies, "G. d'Annunzio University" of Chieti-Pescara, via Luigi Polacchi 11, 66100, Chieti, Italy.
E-mail address: laura.marzetti@unich.it (L. Marzetti).
[1] These authors equally contributed to this work.

https://doi.org/10.1016/j.ynirp.2021.100051
Received 11 January 2021; Received in revised form 4 August 2021; Accepted 6 September 2021
Available online 17 September 2021

series, including e.g. neural generators estimated from measured MEG activity. Indeed, MEG activity in one brain region has multiple time series associated with it. For the estimation of functional connectivity, these multiple time series are typically reduced to a single time series that summarizes the activity in the regions of interest, with potential loss of information. Conversely, relying on multivariate connectivity metrics to assess the coupling between the two regions avoids this potential bias (Basti et al., 2018, 2020).

Alterations of resting-state MEG connectivity are used as a marker of pathology in a number of neurological diseases and neuropsychiatric disorders (e.g., Stam et al., 2006; Greicius, 2008; Gómez et al., 2009; Brunetti et al., 2017; Alamian et al., 2017). Specifically, glioma patients show alterations in functional connectivity (e.g., Bartolomei et al., 2006b; Guggisberg et al., 2008). These alterations are not only restricted to the tumor area but also spread to remote even contralateral areas (Bartolomei et al., 2006b). Despite the interesting findings on spatially specific alterations of activity and connectivity, these studies consider standard frequency bands or broad bands, thus making the interpretation of the results in terms of local and long-range synchronization disputable. In fact, using broad bands does not allow to characterize the functional role of such synchronizations and using fixed bands might bias the results (Donoghue et al., 2021) given the large variability of the e.g. alpha peak frequency across individuals (Haegens et al., 2014), especially when considering subjects with brain lesions (Gloor et al., 1968; Goldensohn, 1979) or in the elderly (Wang and Busse, 1969).

In the present study, we aimed at assessing frequency-specific alterations in brain activity and functional connectivity of the tumor tissue from MEG source space data taking into account individualized frequency bands within the patient group and between patients and age-matched healthy control subjects.

2. Materials and methods

2.1. Participants

Ten consecutive patients (age mean ± st.dev.: 56.3 ± 14.0 years) with a suspected brain glioma on the basis of a MR study participated in this study. Histological diagnosis was obtained by surgical resection or biopsy in all the patients. Patients were eligible if they were adult (≥18 years). Patients' characteristics are summarized in Table 1. In addition, ten age-matched healthy control subjects (age mean ± st.dev.: 54.4 ± 15.0 years) were recruited for the study. Healthy control subjects' characteristics are summarized in Table SM1 of the supplementary material. Age matching between the patient group and the healthy-control-subject group was assessed by using an independent-sample Wilcoxon rank sum test ($p = 0.705$; two-sided test). This research work was conducted in accordance with the Declaration of Helsinki and all procedures were approved by the local Ethics Committee of the University of Chieti-Pescara. All participants (patients and healthy subjects) gave their written informed consent before participation in the experiment.

2.2. MEG data acquisition

MEG recordings were acquired by using the whole-head MEG system installed at the Institute for Advanced Biomedical Technologies (ITAB), University of Chieti-Pescara. This system comprises 153 dcSQUID integrated magnetometers arranged on a helmet-shaped sensor array covering the whole head (Pizzella et al., 2001; Chella et al., 2012). Before entering the MEG shielded room, each participant was asked to remove, as much as possible, metal objects to avoid artifacts during the recording. Five head position indicator (HPI) coils were placed on the participant's head for off-line head-to-MEG-sensor co-registration. To facilitate and speed up the procedure of mounting HPI coils on the patients' head and to induce minimal discomfort, a cap with pre-attached HPI coils was built for this experiment. The positions of the HPI coils relative to three anatomical landmarks (nasion, right and left pre-auricular points) were measured using a Polhemus FastTrack 3D digitizer (Polhemus, Colchester, VT). Two consecutive sessions of 5-min eyes-closed resting-state MEG recordings were acquired, sampled at 1025 Hz; for one patient, only the first session was considered for the analysis since the patient was not able to complete the second session. Each session was followed by 30-s recordings of the magnetic fields generated by the HPI coils. Eye movements and blinks were controlled using vertical electro-oculogram (EOG) recordings, while the heartbeat was monitored through electrocardiogram (ECG) recorded by two electrodes positioned horizontally along the fifth intercostal space in the right and left mid axillary line.

2.3. MRI data acquisition

Magnetic resonance (MR) images were acquired using the 3-T Philips Achieva scanner (Philips Medical Systems, Best, The Netherlands) installed at the Institute for Advanced Biomedical Technologies (ITAB), University of Chieti-Pescara. Imaging protocol is reported in Table 2.

All MR images were first registered to the T1-weighted FFE image without contrast enhancement, and finally co-registered with the MEG data by aligning the anatomical landmarks (nasion, right and left pre-auricular points) identified in the two imaging modalities (MEG and MRI) by using the FieldTrip software toolbox (Oostenveld et al., 2011).

Table 1
Demographic and clinical characteristics of tumor patients. **M** = male; **F** = female; **R** = right; **L** = left; **PL** = parietal lobe; **TPL** = temporo-parietal lobe; **FPL** = fronto-parietal lobe; **FL** = frontal lobe; **S** = splenium; **POL** = parieto-occipital lobe; **TOL** = temporo-occipital lobe; **TL** = temporal lobe; **FTL** = fronto-temporal lobe; **I** = insula; **IDH** = isocitrate dehydrogenase.

Patient no.	Gender	Age (y)	Tumor side	Tumor volume (mm^3)	Tumor location	Tumor type	Tumor grade
1	M	76	R	7039	TL	Glioblastoma; IDH wild-type	IV
2	M	49	L	16046	FPL	Oligodendroglioma; IDH mutant	III
3	F	54	L/R	24516	POL, FL, S	Glioblastoma; IDH wild-type	IV
4	F	52	L	17390	FL	Astrocytoma	II
5	M	39	L/R	37072	PL, FL	Glioblastoma; IDH wild-type;	IV
6	M	59	L	56545	FTL, I	Oligodendroglioma; IDH mutant	III
7	M	51	L	21988	TPL	Glioblastoma; IDH wild-type	IV
8	F	57	L	960	FL	–	II
9	F	84	L	20449	TOL	Glioblastoma; IDH wild-type	IV
10	M	42	R	1123	FL	Glioblastoma; IDH wild-type	IV

Table 2
Imaging protocol parameters.

Sequence	Parameters
Pre- and post-gadolinium enhanced three-dimensional fast-field-echo (FFE) T1-weighted	Sagittal acquisition; repetition time (ms)/echo time (ms), 7.6/3.7; slice thickness, 1 mm; matrix, 256 × 256
Fluid-attenuated inversion recovery	3-mm axial acquisition; 11000/125; inversion time (ms), 2800; matrix, 320 × 200

2.4. MEG data analysis

The following subparagraphs summarize the main steps of the MEG data analysis pipeline performed in this study. Most analyses (i.e., from pre-processing to source estimation) were performed using the FieldTrip software toolbox. An in-house made Matlab code was employed for MEG source functional connectivity analysis.

2.4.1. MEG data pre-processing

Raw MEG signals were band-pass filtered at 1–100 Hz. Notch filters at 50 and 100 Hz were also used to suppress power line interference. The filtered MEG signals were visually inspected, and the segments of signal containing large artifacts originating from eye movements, blinks, muscular activity or SQUID jumps were removed (Gross et al., 2013). An independent component analysis (ICA) (Hyvärinen and Oja, 2000) was also applied for instrumental and biological artifact removal. Specifically, ICA was performed by using the FastICA algorithm, with deflationary orthogonalization and tanh non-linearity. ICA was repeated multiple times (i.e., 40) starting from different randomly generated initial conditions. For each repetition, the extracted independent components (ICs) were classified as artifactual components or components of brain origin by using a custom-made adaptation of the Human Connectome Project fully-automated classification procedure (Larson-Prior et al., 2013), followed by visual inspection to correct possible IC misclassifications. The repetition with the largest number of brain components and the lowest artifact residual was retained as the best IC decomposition and used for artifact removal. The average number of ICs classified as artifactual components was 9.9 (range: [minimum, maximum] = [5, 20]). The clean MEG signals were used as input to subsequent steps of the analysis pipeline.

2.4.2. MEG forward model

Building the MEG forward model is the first step toward the estimation of the neural sources that generated the observed MEG signals. It involves the calculation of the magnetic fields generated from known current sources. In this study, the MEG forward model was built for current-dipole-like sources located within the brain volume, by using a realistically shaped head model and the Boundary Element Method (BEM) approach (Hämaläinen and Sarvas, 1989; Mosher et al., 1999). To this end, surface meshes for the outer boundaries of the scalp, skull, and intracranial volume were extracted from the segmentation of T1-weighted FFE images. From these meshes, a realistically shaped three-shell head model was constructed, comprising the intracranial volume (i.e., the brain and CSF), the skull, and the scalp. Tissue conductivities were set to 0.33 S/m for the scalp, 0.0066 S/m for the skull, and 0.33 S/m for the intracranial volume. The MEG forward model was finally built for three unit-strength orthogonal dipoles located at each vertex of a 4-mm-spaced grid covering the intracranial volume by using the BEM solver implemented in FieldTrip (Gramfort et al., 2010), resulting in a lead field matrix whose columns contain the sensor topographies of the magnetic field generated by each dipolar source. The average number of source-grid vertices across subjects was 24342 (range: [minimum, maximum] = [18325, 31281]).

2.4.3. MEG source estimation

Brain source activity was estimated from the clean MEG signals using a vector-type minimum-variance (MV) beamformer with unit-noise-gain constraint (Borgiotti and Kaplan, 1979). This approach was chosen since it has no location bias and it attains a significantly larger spatial resolution than other MV beamformer approaches (Sekihara and Nagarajan, 2008). We emphasize that a vector-type formulation of the beamformer results in a vector-type activity with three components, i.e., one for each orthogonal spatial direction, at each source location.

For each source element i (that is, for each vertex of the 4-mm-spaced source grid), a $N_{ch} \times 3$ vector-type spatial filter $\boldsymbol{W}_i$, with N_{ch} being the number of MEG channels, was constructed by using an estimate of the measurement covariance matrix in the frequency range 1–30 Hz, as (Sekihara et al., 2001; Sekihara and Nagarajan, 2008)

$$\boldsymbol{W}_i = \boldsymbol{C}^{-1}\,\boldsymbol{L}_i\left[\boldsymbol{L}_i^T\,\boldsymbol{C}^{-1}\,\boldsymbol{L}_i\right]^{-1}\begin{bmatrix}\Upsilon_{11}^{-1/2} & 0 & 0\\ 0 & \Upsilon_{22}^{-1/2} & 0\\ 0 & 0 & \Upsilon_{33}^{-1/2}\end{bmatrix} \tag{1}$$

where the $N_{ch} \times 3$ matrix $\boldsymbol{L}_i$ is the local lead-field matrix (i.e., a three-column matrix whose columns contain the sensor topographies of the magnetic field generated by three unit-strength orthogonal dipoles at location i), $\boldsymbol{C}$ is the $N_{ch} \times N_{ch}$ measurement covariance matrix, the superscripts T and -1 denote the transpose and inverse operator, respectively, and Υ_{11}, Υ_{22} and Υ_{33} are the diagonal entries of the 3×3 matrix

$$\boldsymbol{\Upsilon} = \left[\boldsymbol{L}_i^T\,\boldsymbol{C}^{-1}\,\boldsymbol{L}_i\right]^{-1}\boldsymbol{L}_i^T\,\boldsymbol{C}^{-2}\,\boldsymbol{L}_i\left[\boldsymbol{L}_i^T\,\boldsymbol{C}^{-1}\,\boldsymbol{L}_i\right]^{-1} \tag{2}$$

The vector-type activity of source element i at a given time instant t was finally estimated as weighted sum of sensor measurements $\boldsymbol{x}(t)$, i.e.,

$$\boldsymbol{s}_i(t) = \boldsymbol{W}_i^T\boldsymbol{x}(t) \tag{3}$$

where the vectors $\boldsymbol{x}(t)$ and $\boldsymbol{s}_i(t)$ have dimensions $N_{ch} \times 1$ and 3×1, respectively.

2.4.4. MEG source power analysis

Source power estimated by using the MV beamformer with unit-noise-gain constraint is equal to the power of the source activity normalized by the power of source-level noise due to additive sensor noise (Sekihara et al., 2001). For each component of the vector-type source activity in equation (3), this is equivalent to the neural activity index (NAI) introduced by Van Veen et al. (1997) in the case of uncorrelated white sensor noise. For this reason, we will hereinafter refer to the estimated source power as NAI.

To estimate source NAI in a frequency band of interest F (see section 2.5.1 for the selection of frequency bands), we first computed the $N_{ch} \times N_{ch}$ data cross-spectral density matrix, $\boldsymbol{S}_x(F)$, by using a multi-taper approach (i.e., orthogonal Slepian tapers) which is optimal for averaging spectral estimates over a frequency range (Percival and Walden, 1993). We then projected cross-spectral density from the sensor-level to the source-level through the beamformer spatial filters, i.e.,

$$\boldsymbol{S}_{ii}(F) = \boldsymbol{W}_i^T\,\boldsymbol{S}_x(F)\,\boldsymbol{W}_i \tag{4}$$

for the 3×3 cross-spectral density matrix of the vector-type activity of source element i, or

$$\boldsymbol{S}_{ij}(F) = \boldsymbol{W}_i^T\,\boldsymbol{S}_x(F)\,\boldsymbol{W}_j \tag{5}$$

for the 3×3 cross-spectral density matrix between the vector-type activities of source elements i and j.

For each source element i, NAI was estimated as follows:

$$\mathrm{NAI}_i(F) = Tr\{\,\boldsymbol{S}_{ii}(F)\,\} \tag{6}$$

where $Tr\{\cdot\}$ denotes the trace operator.

2.4.5. MEG source connectivity analysis

Functional connectivity between brain sources was assessed in terms of Multivariate Interaction Measure (MIM) (Ewald et al., 2011). This method is a generalization of the imaginary part of coherence (Nolte et al., 2004) for estimating functional connectivity between multivariate time series, such as vector-type activity estimated at each source location in this study. This method does not catch non-linear cross-frequency brain functional connectivity (e.g., Chella et al., 2017) the detection of which id beyond of the scope of this work.

Similarly to the imaginary part of coherence, MIM does not lead to artifactual connectivity detections due to source leakage, crosstalk, or volume conduction in EEG and MEG (Marzetti et al., 2019).

For each pair of source elements i and j, MIM in a frequency band of interest F was estimated as follows (Ewald et al. 2011)

$$\mathrm{MIM}_{ij}(F) = Tr\left\{ \left[\boldsymbol{S}_{ii}^{\Re}(F)\right]^{-1} \boldsymbol{S}_{ij}^{\Im}(F) \left[\boldsymbol{S}_{jj}^{\Re}(F)\right]^{-1} \left[\boldsymbol{S}_{ij}^{\Im}(F)\right]^{T} \right\} \quad (7)$$

where the superscripts $\Re$ and $\Im$ denote the real and imaginary parts of a complex-valued matrix, respectively.

2.5. Group analysis and statistics

2.5.1. Selection of individual frequency bands

Since a bulk of evidence in the literature demonstrated a 'slowing down' of the alpha rhythms due to brain lesions or aging (Gloor et al., 1968; Wang and Busse, 1969; Goldensohn, 1979), frequency bands were defined according to the individual alpha frequency (IAF) (Klimesch, 1999). For each patient or healthy subject, source locations were first mapped onto the Automated Anatomical Labeling atlas (Tzourio-Mazoyer et al., 2002), and occipital sources were identified as those belonging to parcels within the occipital lobe. IAF was then calculated as the frequency with maximal NAI in occipital sources in the extended alpha range 7–13 Hz, sampled with 0.5 Hz frequency resolution. Based on the IAF, the following individual frequency bands were considered: delta from 1 Hz to 4 Hz, theta from 4 Hz to IAF-3 Hz, lower alpha from IAF-3 Hz to IAF, upper alpha from IAF to IAF+3 Hz, and beta from IAF+3 Hz to IAF+17 Hz, subject to the constraint that the upper bound of upper alpha (or the lower bound of beta) did not exceed 13 Hz, and that the lower bound of lower alpha (or the upper bound of theta) did not go below 6 Hz.

2.5.2. Within-patients analysis

A board-certificated physician interpreted patients' contrast-enhanced T1-weighted and FLAIR images and provided, for each patient, a binary segmentation of the tumor volume (tumor mask) by using the ITK-SNAP software toolbox (Yushkevich et al., 2016). MRI images were then warped to the MNI template brain (Fonov et al., 2009, 2011) by using the SPM software toolbox (http://www.fil.ion.ucl.ac.uk). Specifically, the non-linear warping transformation was determined using the T1-weighted image without contrast enhancement and then applied to all the other MR images, including the tumor mask, to bring them in the MNI space. Based on MNI-warped images of the brain and of the tumor mask, we selected individual regions of interest (ROIs) as follows i) a tumor region, identified as the volume covered by the tumor mask; ii) a peritumor region, identified as the volume within 20-mm distance (measured in the MNI space) from the outer boundary of the tumor region (Lizarazu et al., 2020); iii) a contralateral region and a peri-contralateral region, identified as the symmetric reflection (in the MNI space) with respect to the midsagittal plane of the tumor region and the peritumor region, respectively; and iv) the 'rest of the brain', identified as the volume not included in the other ROIs. For patients with unilateral tumor (8 out of 10), we checked that the peri-tumor and peri-contralateral regions were confined to one hemisphere and did not cross to the other hemisphere. For patients with bilateral tumor (2 out of 10), we checked that the contralateral and peri-contralateral regions did not overlap with the tumor and peritumor regions. Fig. 1 shows an example of these ROIs in one representative patient.

To perform a within-patients analysis of brain activity and functional connectivity, we computed measures of power and global functional connectivity for each of the above selected ROIs. Specifically, for each frequency band of interest F, NAI was averaged across source elements within the same ROI to get a measure of total ROI power.

For the analysis of functional connectivity, we first computed a global MIM value (GMIM) for each source element i as the average of MIM values assessing functional connectivity between the source element i and all possible source elements within the 'rest of the brain' region, i.e.,

$$\mathrm{GMIM}_i(F) = \frac{1}{N_R} \sum_{j \in \textit{Rest of the brain}} \mathrm{MIM}_{ij}(F) \quad (8)$$

where N_R is the number of source elements within the 'rest of the brain'. GMIM values were then averaged across source elements within each ROI to get a measure of global functional connectivity between the ROI and the 'rest of the brain'.

NAI and GMIM values in each ROI were averaged across the two recording sessions. We finally looked at the relative difference for NAI and GMIM in two given ROIs as

$$\text{Relative difference for } \mathrm{NAI}_{XY}(F) = \frac{\mathrm{NAI}_X(F) - \mathrm{NAI}_Y(F)}{\mathrm{NAI}_X(F) + \mathrm{NAI}_Y(F)} \quad (9)$$

and

$$\text{Relative difference for } \mathrm{GMIM}_{XY}(F) = \frac{\mathrm{GMIM}_X(F) - \mathrm{GMIM}_Y(F)}{\mathrm{GMIM}_X(F) + \mathrm{GMIM}_Y(F)} \quad (10)$$

where X and Y indicate the two ROIs. Specifically, X and Y represent target regions (i.e., tumor region, peri-tumor region), and control regions (i.e., the 'rest of the brain', tumor and peri-tumor contralateral regions). The choice of the tumor and peri-tumor contralateral regions as control regions, in addition to the 'rest of the brain', has been inspired by the consideration that these regions share similar geometrical properties with the tumor and peri-tumor regions, e.g., spatial extent, depth with respect to the MEG sensor array.

The statistical significance of the observed relative differences for NAI or GMIM in two ROIs was assessed by using a paired-sample permutation test (Good, 1994) with 10,000 random permutations. Correction for multiple comparison was performed using the

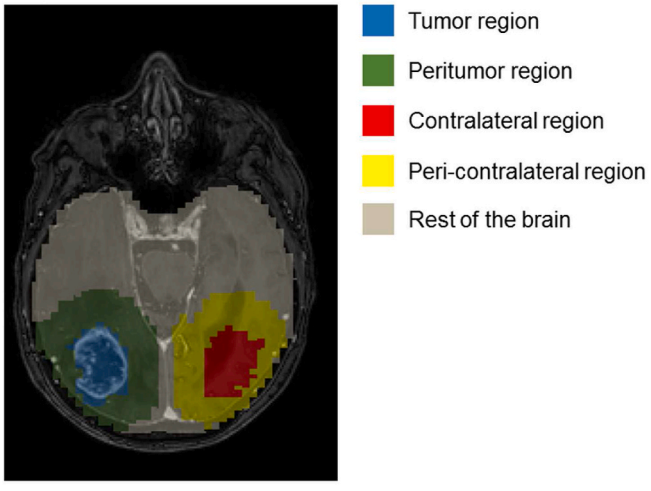

Fig. 1. Illustrative example of regions of interest (ROIs) in one representative patient with a tumor in the left temporo-occipital lobe. The figure shows an axial cross-sectional image of the ROIs superimposed on the T1-weighted MR image with contrast enhancement.

false-discovery-rate (FDR) approach (Benjamini and Yekutieli, 2001).

2.5.3. Comparison of brain tumor patients with healthy controls

Tumor patients and healthy subjects were first compared in terms of whole-brain band relative power and functional connectivity. Specifically, we considered the whole brain volume as region of interest and, for each frequency band, we computed a whole-brain band-relative NAI as the average NAI across all sources in the brain, as well as across the two recording sessions, eventually normalized by the broadband NAI (from 1 Hz to the upper bound of the individual beta band), i.e.,

$$\mathrm{rNAI}_{whole\ brain}(F) = \sum_i \mathrm{NAI}_i(F) \Big/ \sum_i \mathrm{NAI}_i(F_{broad-band}) \tag{11}$$

where the index i runs over all sources in the brain. The normalization with the broadband NAI was required to remove individual absolute power biases due, e.g., to the volume conductor properties, that could affect the group comparison. Similarly, we computed a whole-brain GMIM as the average GMIM across all sources in the brain, as well as across the two recording sessions.

To investigate hemispheric differences in global functional connectivity, we first calculated the average GMIM within each hemisphere, i.e., $\mathrm{GMIM_{LH}}$ for the left hemisphere and $\mathrm{GMIM_{RH}}$ for the right hemisphere, and then we evaluated the differences between the left hemisphere and the right hemisphere as follows

$$\mathrm{GMIM\ \ hemispheric\ \ difference} = |\mathrm{GMIM_{LH}} - \mathrm{GMIM_{RH}}|. \tag{12}$$

We also evaluated a laterality index (LI) as follows (Seghier, 2008)

$$\mathrm{LI} = \left|\frac{\mathrm{GMIM_{LH}} - \mathrm{GMIM_{RH}}}{\mathrm{GMIM_{LH}} + \mathrm{GMIM_{RH}}}\right| \tag{13}$$

A laterality index near zero indicates nearly symmetrical or bilateral global functional connectivity; higher values indicate more lateralized global functional connectivity. Of note, both the hemispheric difference in the GMIM and the laterality index were considered in absolute value in order to pool together patients who either had right- or left-hemisphere tumor, as well as healthy control subjects for which no impairment exists.

The statistical significance of the observed differences for whole-brain rNAI, whole-brain GMIM, or GMIM hemispheric difference in the patient group and healthy control group was assessed by using an independent-sample permutation test with 10,000 random permutations. Correction for multiple comparison was performed using the FDR approach.

3. Results

3.1. Alpha frequency peak differs between patients and healthy subjects

The individual alpha frequency (IAF), defined as the frequency with maximal NAI in occipital sources in the extended alpha range 7–13 Hz, was calculated separately for patients' and healthy subjects' groups ($\mathrm{IAF_P}$ and $\mathrm{IAF_H}$, respectively) leading to average values (mean ± st. dev.) equal to $\mathrm{IAF_P} = (8.8 \pm 1.2)$ Hz and to $\mathrm{IAF_H} = (10.5 \pm 0.9)$ Hz; data are shown in figure SM3. The IAF values of the patients were significantly lower than those of the control subjects (one-tailed Mann-Whitney U test, $p = 0.002$).

3.2. Tumor and peri-tumor regions feature lower power in the alpha and beta bands with respect to the rest of the brain

Fig. 2a shows the relative difference for Neural Activity Index (NAI), as defined in Eq. (9), between i) the tumor region and peri-tumor regions pooled together (i.e., 'Tumor and Peritumor') and the rest of the brain (i.e., 'Rest of the brain'); ii) the pooled corresponding contralateral regions (i.e., 'Contralateral') and the 'Rest of the brain'; and iii) 'Tumor and Peritumor' and 'Contralateral' for all the frequency bands taken into account. Results in Fig. 2a as well as in Fig. 3a, Fig. 4a and b and in the SM figures, are visualized using violin-plots (Hintze and Nelson, 1998.), an approach that, by visualizing summary statistics and density shape into a single plot, provides maximally transparent statistical information, in comparison to e.g. plotting mean or median barplots and error-bars (Allen et al., 2019).

Statistical significance was assessed by using a paired-sample permutation test with 10,000 random permutations. The choice of pooling together the tumor and peritumor regions as well as their respective contralateral regions has been driven by the analysis, reported in Figures SM1 and SM2 of the supplementary material, showing that these

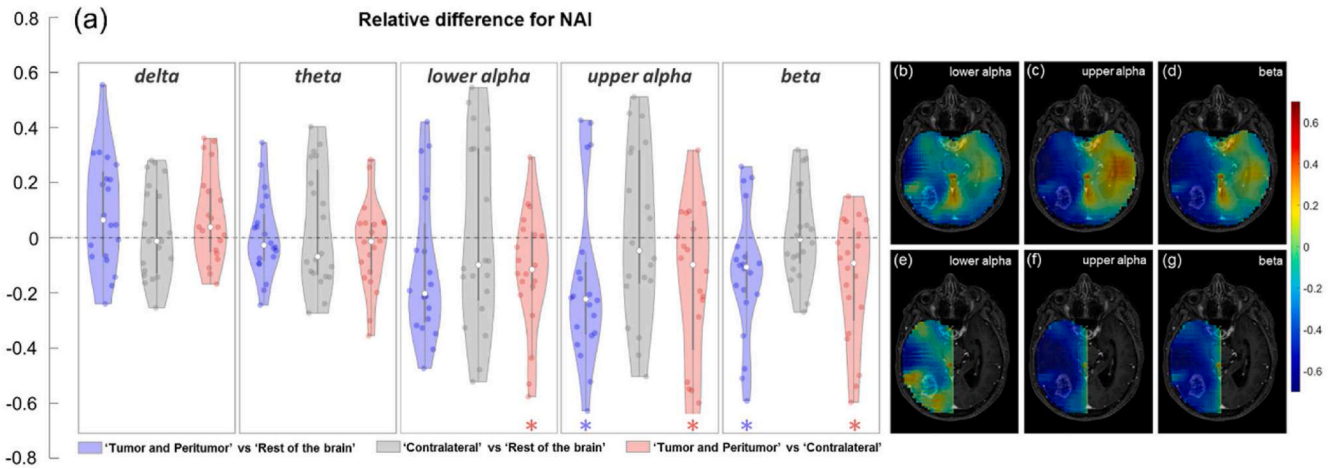

Fig. 2. (a) Violin plots of the relative difference for Neural Activity Index (NAI) in the pooled tumor- and peritumor regions 'Tumor and Peritumor' compared to the rest of the brain 'Rest of the brain' and to contralateral control regions 'Contralateral', and in the contralateral control regions compared to the rest of the brain; the white dot and the thick whiskers denote the median value across patients and the range from the 25th to the 75th percentile, respectively; the symbol * denotes a significant difference at the $p < 0.05$ level (paired-sample permutation test, one-tail, FDR corrected). (b, c, d): axial cross-sectional maps of the relative difference for NAI at each brain location compared to the 'Rest of the brain', for the lower alpha, upper alpha and beta frequency bands, in one representative patient with a glioma in the left temporo-occipital lobe; the maps are superimposed on the T1-weighted MR image with contrast enhancement. (e, f, g): axial cross-sectional maps from the same patient of the relative difference for NAI in each location within the hemisphere ipsilateral to the tumor compared to its homologous location in the hemisphere contralateral to the tumor. A substantial decrease in NAI can be observed in the region within and surrounding the tumor compared to the rest of the brain, as well as to the contralateral region, in the lower alpha, upper alpha and beta frequency bands.

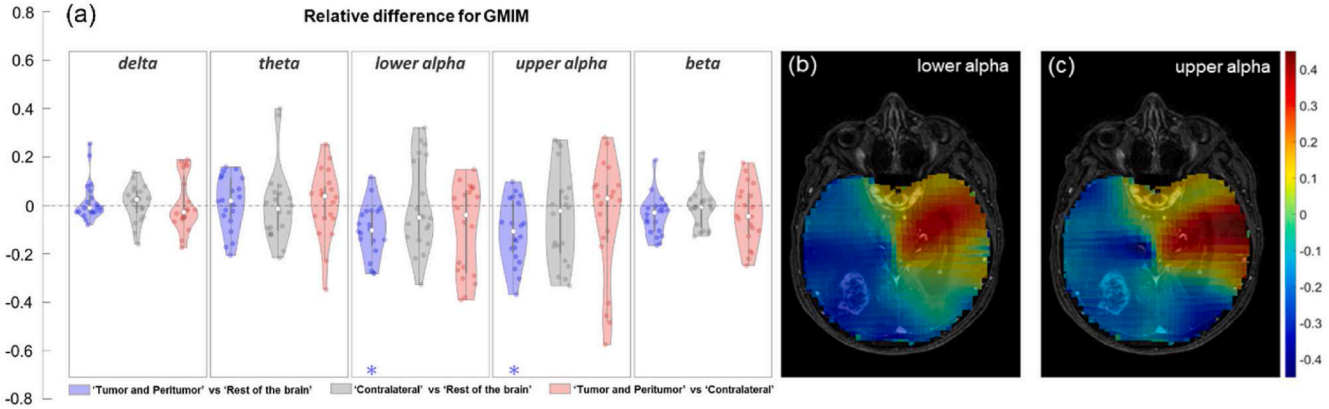

Fig. 3. (a) Violin plots of the relative difference for the Global Multivariate Interaction Measure (GMIM) in the pooled tumor and peritumor regions 'Tumor and Peritumor' compared to the rest of the brain 'Rest of the brain' and to contralateral control regions 'Contralateral', and in the contralateral control regions compared to the rest of the brain; the white dot and the thick whiskers denote the median value across patients and the range from the 25th to the 75th percentile, respectively; the symbol * denotes a significant difference at the $p < 0.05$ level (paired-sample permutation test, one-tail, FDR corrected). (b, c): axial cross-sectional maps of the relative difference for GMIM in each brain location compared to the rest of the brain, for the lower alpha and upper alpha frequency bands, in one representative patient with a glioma in the left temporo-occipital lobe; the maps are superimposed on the T1-weighted MR image with contrast enhancement. A substantial decrease of GMIM can be observed in the region within and surrounding the tumor compared to rest of the brain in the lower alpha and upper alpha frequency bands.

pairs of regions do not exhibit differences in their activity and connectivity in any of the frequency bands. Our results show that 'Tumor and Peritumor' regions feature a NAI value significantly lower than that of the 'Rest of the brain' in the upper alpha ($p = 0.044$, FDR corrected) and beta ($p = 0.041$, FDR corrected) frequency bands; a similar trend was observed in the lower alpha band, although this comparison did not reach statistical significance. This decrease of NAI is still observed in the lower alpha ($p = 0.042$, FDR corrected), upper alpha ($p = 0.041$, FDR corrected) and beta ($p = 0.039$, FDR corrected) frequency bands when 'Tumor and Peritumor' regions are compared to 'Contralateral', suggesting that, as indicated by the direct comparison between 'Contralateral' and the 'Rest of the brain', there is no power modulation in the 'Contralateral' regions with respect to the 'Rest of the brain' in any of these frequency bands. Illustrative examples from one representative patient of the maps of the relative difference for NAI are given in Fig. 2b–g.

3.3. Tumor and peri-tumor regions feature an alpha band functional connectivity lower than the rest of the brain

Fig. 3 shows the relative difference for GMIM, as defined in Eq. (10), between i) 'Tumor and Peritumor' and 'Rest of the brain'; ii) 'Contralateral' and the 'Rest of the brain'; and iii) 'Tumor and Peritumor' and 'Contralateral' for all the frequency bands taken into account. These relative differences show that, while for the delta and theta frequency bands no relevant spatial modulation of functional connectivity can be observed, in the lower and upper alpha bands a clear decrease in functional connectivity within the 'Tumor and Peritumor' region compared to the 'Rest of the brain' is displayed ($p = 0.002$ and $p = 0.003$, respectively, FDR corrected). This alpha band decrease was confirmed when 'Tumor and Peritumor' functional connectivity is compared to 'Contralateral' functional connectivity, although this comparison did not reach statistical significance. Finally, the beta band functional connectivity within the 'Tumor and Peritumor' region showed a trend similar to that of lower and upper alpha functional connectivity. Illustrative examples from one representative patient of the maps of the relative difference for GMIM are given in Fig. 3b–c.

3.4. Brain tumor patients feature a global enhancement in lower-alpha band power with respect to control subjects

The analysis of Neural Activity Index modulations between control subjects and tumor patients shows (Fig. 4, left panel) that whole-brain band-relative power in tumor patients is higher than in control subjects in the lower-alpha frequency band ($p = 0.02$, independent-sample permutation test, one-tail, FDR corrected). Additionally, we observed a beta band reduction in power in tumor patients with respect to control subjects ($p = 0.04$, independent-sample permutation test, one-tail, uncorrected), which did not survive FDR correction. For the other frequency bands, differences between tumor patients and control subjects did not reach statistical significance even without FDR correction.

For connectivity analysis, differences in the GMIM calculated for the whole brain for the delta, theta, lower alpha, upper alpha, and beta frequency bands were tested between brain tumor patients and healthy control subjects (Fig. 4, right panel). Overall, our results suggest a theta and lower-alpha enhancement in global functional connectivity in tumor patients with respect to control subjects (theta: $p = 0.02$, lower alpha: $p = 0.04$, independent-sample permutation test, one-tail, uncorrected), which did not survive FDR correction.

Additionally, the analysis of hemispheric differences in the GMIM shows (Fig. 5, left panel) a significant increase of GMIM hemispheric difference in the theta band for tumor patients as compared to control subjects ($p = 0.04$, independent-sample permutation test, one-tail, uncorrected), which did not survive FDR correction. Modulations of GMIM hemispheric difference in the other frequency bands did not reach statistical significance, even without FDR correction. Interestingly, in tumor patients, the increased laterality of GMIM in the theta band is negatively correlated with the tumor volume (Spearman's rho $= -0.62$, $p = 0.03$, one-sided Spearman's rank correlation test).

4. Discussion

In the present study, we show that brain tumors affect oscillatory brain activity and functional connectivity by decreasing Neural Activity Index in tumor and peri-tumor regions in the upper-alpha and beta bands, paired to decreasing global Multivariate Interaction Measure of the tumor and peri-tumor regions in lower and upper-alpha band. Additionally, when compared to age-matched healthy subjects, patients feature a global enhancement of power in the lower-alpha band.

Importantly, in this study, the frequency bands used for power and functional connectivity analyses are defined starting from Individual Alpha Frequency (IAF). Indeed, in our study occipital IAF values were found to be significantly different between patients and controls, with values for controls that are in line with previous literature for resting-

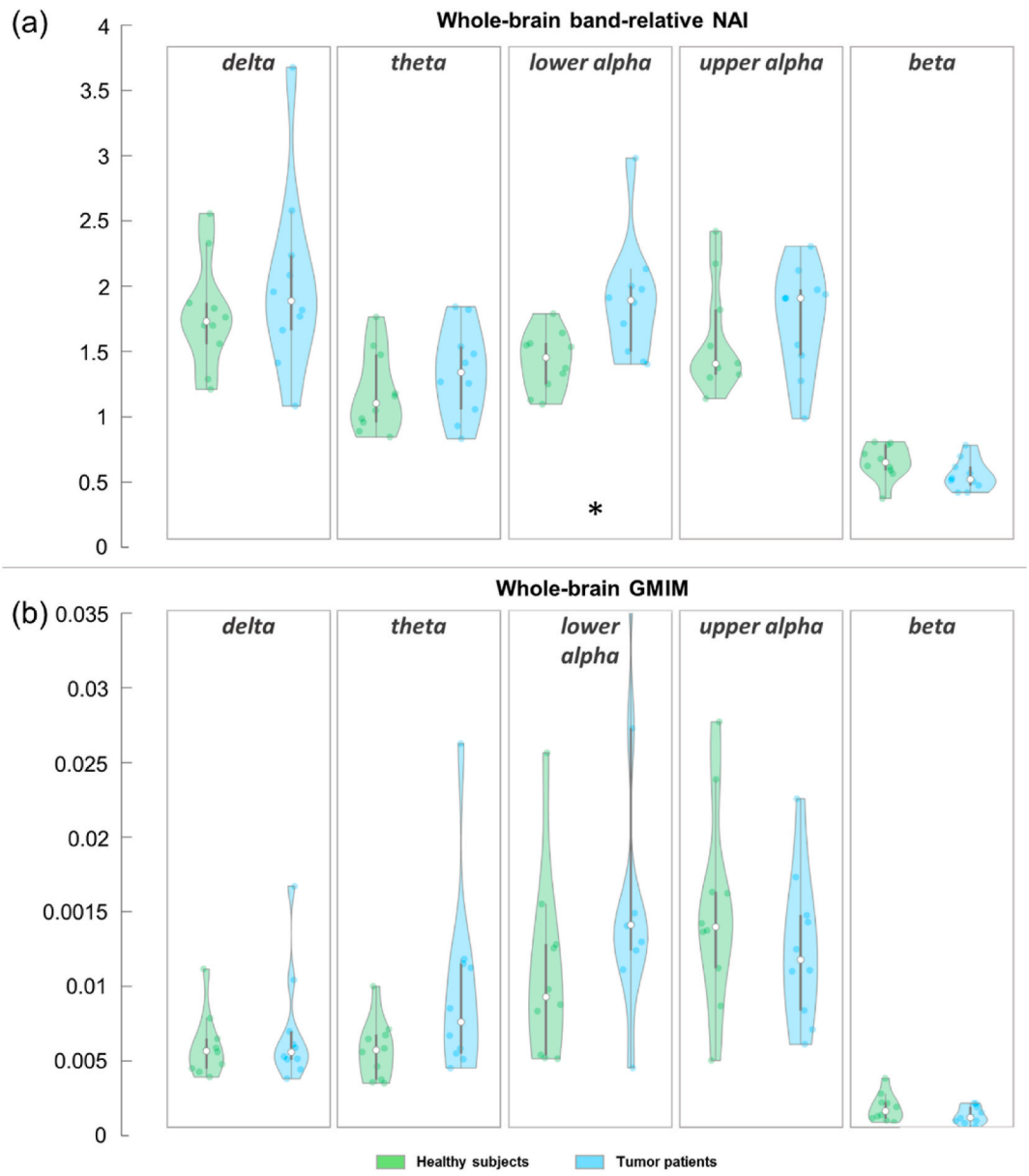

Fig. 4. (a) Violin plots of the average band-relative Neural Activity Index (NAI) in the whole brain for healthy subjects and tumor patients. The white dot and the thick whiskers denote the median value across patients and the range from the 25th to the 75th percentile, respectively. The symbol * denotes a significant difference at the $p < 0.05$ level (independent-sample permutation test, one-tail, FDR corrected). A significant increase of average band-relative NAI in the lower-alpha band can be observed in the whole brain of tumor patients compared to healthy subjects. (b) Average Global Multivariate Interaction Measure (GMIM) in the whole brain for healthy subjects and tumor patients.

state occipital alpha peak (Haegens et al., 2014) and values for patients that are significantly lower, as expected from previous studies on brain lesions (Gloor et al., 1968), in line with poorer cognitive functions in patients with respect to age-matched healthy subjects (Bosma et al., 2008b).

To the best of our knowledge, the vast majority of MEG studies on patients with brain tumors either consider broad band activity and connectivity (Bartolomei et al., 2006a), making it almost impossible to infer the role of the different frequency bands in abnormal brain communication (Schnitzler and Gross, 2005), or, when using selected frequency bands, do not take into account individualized frequency peak values and bands. Additionally, several of these studies consider MEG activity and connectivity at channel level, i.e. of sensor level MEG data, and infer spatially specific differences by averaging results across sensors in a cluster (e.g., temporal, parietal) without taking into account the different spatial location of tumors across patients (Bosma et al., 2008a, b; Bartolomei et al., 2006a, b).

Conversely, in this study, frequency-specific power and functional connectivity were calculated in the bands defined on the basis of IAF values for patients and control subjects, and for each patient, power and connectivity in the tumor and peritumor regions were compared to the same quantities for the rest of the brain or for the corresponding contralateral regions.

With this approach, in the patient group, we observed a significant decrease in power in tumor and peri-tumor regions in the lower-alpha, upper-alpha and beta bands (Fig. 2). These findings are in line with the electrocorticographic study by Bandt et al. (2017) where a power reduction has been observed within the tumor at the mu and beta frequencies, possibly indexing a thalamico-cortical disconnection.

Although not significant, we also observed a tendency towards an enhancement of delta power in tumor and peritumoral regions consistent with previous literature (e.g., Baayen et al., 2003; De Jongh et al.,

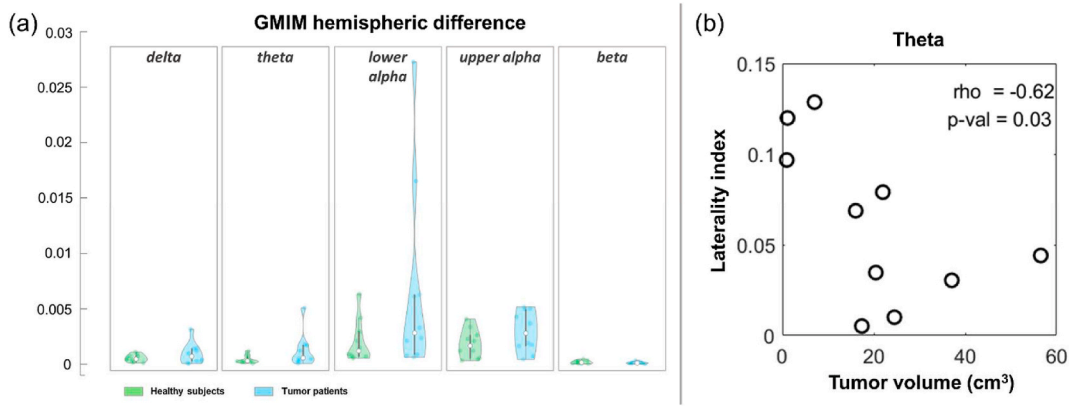

Fig. 5. (a) Violin plots of the GMIM hemispheric difference for healthy subjects and tumor patients. (b) Negative correlation of GMIM laterality index in the theta band with the tumor volume (Spearman's rho = −0.62, p = 0.03, one-sided Spearman's rank correlation test).

2003; Oshino et al., 2007). Our beta band power findings are in line with van Wijk et al. (2012) showing a decrease in beta power in the primary motor area of the tumor hemisphere compared to the contralateral area in the resting-state. In contrast to this study, we did not observe an enhancement of the mu-rhythm rather a decrease in alpha power, possibly driven by occipital alpha rather than by Rolandic alpha (mu-rhythm).

Our results for functional connectivity in the patient group (Fig. 3) point towards a significant decrease in the tumor and peritumor regions in the lower- and upper-alpha bands with respect to the rest of the brain and a tendency in the comparison to the contralateral region. Interestingly, a similar lowering of functional connectivity in tumor and peritumoral regions in the alpha band has been associated with a lower rate of post-operative neurological deficits (Guggisberg et al., 2008; Tarapore et al., 2012) and to the absence of eloquent cortex during intraoperative electrical stimulation (Martino et al., 2011). Along the same line, resection of brain areas featuring high functional connectivity in the alpha-band is related to post-operative deficits in Lee et al. (2020). Alpha band connectivity has also been shown to increase in resting-state brain networks in patients after tumor resection (van Dellen et al., 2013). In their study, van Dellen et al. (2013) found that post-resection increase in low-alpha band connectivity is positively correlated with working memory performance, while post-resection increases in the upper-alpha band connectivity is positively correlated with attention. Our results for a decrease in functional connectivity in the tumor in lower- and upper-alpha bands are in line with the above findings and suggest the possibility of improving specific cognitive performance in our patient population if the tumor is removed.

The comparison between patients and age-matched healthy control subjects (Fig. 4) highlighted that patients feature a global enhancement of power in the lower-alpha band with respect to controls, paired to an indication for a global reduction of power in the beta band.

The comparison between patients and age-matched healthy control subjects also suggested a global enhancement of functional connectivity in the theta and lower-alpha bands in patients. Of note, this enhancement cannot be explained by antiepileptic drugs (Levetiracetam in 3 patients) since previous EEG evidence shows that patients taking Levetiracetam feature a reduction of global and regional functional connectivity with respect to controls (Ricci et al., 2021).

Interestingly, in the theta band, such a global enhancement was paired to an increase of the hemispheric difference of functional connectivity. Our finding that the hemispheric lateralization of functional connectivity decreases with the tumor volume suggests that the effects of the tumor are local and asymmetrically located in the two hemispheres if the tumor is small, and more widespread in the brain if the tumor is large. Previous studies along the same line have shown that functional connectivity in brain tumor patients is enhanced with respect to controls in the delta, alpha, and beta frequency bands and reduced in gamma (Bartolomei et al., 2006b), and in the theta frequency band (Bartolomei et al., 2006b). Nevertheless, the gamma band used by Bartolomei et al. (2006b) partly overlaps to our definition of individual beta bands, thus possibly reconciling our beta band findings with their gamma band findings. Our findings for lower-alpha functional connectivity decrease in the tumor and peri-tumor regions suggest that the whole-brain connectivity increase observed with respect to control subjects is possibly due to increased functional connectivity in non-tumor (and non-peri-tumor) regions.

It should be noted that considering fixed frequency bands may lead to different results and conclusions compared to those obtained considering individualized frequency bands. In figure SM4 of the supplementary material, we show the results of the comparison between patients and healthy control subjects obtained by using the traditional frequency bands: delta from 1 Hz to 4 Hz, theta from 4 Hz to 7 Hz, lower alpha from 7 Hz to 10 Hz, upper alpha from 10 Hz to 13 Hz, and beta from 13 Hz to 30 Hz. Since the IAF of tumor patients is significantly lower than the IAF of healthy control subjects (one-tailed Mann-Whitney U test, p = 0.002), the traditional frequency bands are differently aligned with respect to the IAF in the two groups being compared (i.e., tumor patients and healthy control subjects). Moreover, since the IAF of tumor patients is significantly lower than 10 Hz (one-sided Wilcoxon signed rank test, p = 0.012), the traditional upper-alpha band misses most of the real upper-alpha band and contains part of the real beta band; similarly, the traditional theta band misses part of the real theta band and contains part of the real lower-alpha band. On the other hand, the IAF of healthy control subjects does not significantly differ from 10 Hz (one-sided Wilcoxon signed rank test, p = 0.082). As a consequence, the traditional bands firstly suggest an upper-alpha reduction in global functional connectivity in tumor patients with respect to control subjects (p = 0.02, independent-sample permutation test, one-tail, uncorrected) which is not revealed by the individual frequency bands (p = 0.17, independent-sample permutation test, one-tail, uncorrected); secondly, they miss the theta enhancement in global functional connectivity in tumor patients with respect to control subjects (p = 0.091, independent-sample permutation test, one-tail, uncorrected) which is only revealed by the individual frequency bands (p = 0.02, independent-sample permutation test, one-tail, uncorrected); lastly, they suggest a trend of upper-alpha reduction in power in tumor patients with respect to control subjects (Figure SM4a), which is the opposite of the upper-alpha enhancement revealed by the individual frequency bands (Fig. 4a). Overall, the choice of fixed frequency bands has smaller effects on the results of the within-patient analysis (see Figure SM5) as compared to those of the comparison between patients and healthy subjects, since the 90% of the tumor patients has the IAF within the traditional lower-alpha band (8–10 Hz) and, thus, the within group variability for IAF is smaller

than the between group variability (ANOVA: mean square between groups = 1.09, mean square between groups = 14.45).

Altogether, the present study supports the idea that gliomas affect not only brain activity and connectivity in the proximity of the tumor, but also impact on oscillatory power and functional connectivity in regions located remotely from the tumor, suggesting a network level effect induced by a spatially confined lesion. The frequency specificity of our findings is possibly related to different altered cognitive domains. Indeed, about 90% of brain tumor patients experience severe neuropsychological impairments both for HGG (Klein et al., 2001, 2003) and for LGG patients (Reijneveld et al., 2001; Taphoorn et al., 1994; Taphoorn and Klein, 2004). These disturbances are usually global and can hardly be explained only by a local damage caused by the tumor rather by a network level effect.

It has been shown that brain tumor tissue exhibits a different conductivity than healthy brain tissue; in general, the conductivity of low-grade gliomas is higher than the one of healthy tissue, while the conductivity of higher-grade gliomas is lower (Rajshekhar, 1992; Latikka and Eskola, 2019). Despite these differences, in the present study we neglected any heterogeneity of brain tissues and we limited ourselves to a realistically-shaped three-shell head model comprising homogeneous compartments for the skin, the skull, and the intracranial volume, for the following reasons. Firstly, due to properties of magnetic fields in near-spherical geometry, MEG mainly reflects the primary neuronal (or intracellular) currents and to a lesser extent the volume (or extracellular) currents (Hämäläinen et al., 1993; Niedermeyer and Lopes da Silva, 2005). This makes MEG less sensitive to forward modeling errors as compared to EEG (Stenroos et al., 2014). To date, the standard approach to head modeling in experimental MEG studies is to use a realistically-shaped single-shell model comprising only one homogeneous compartment for the intracranial volume.; this model has been shown to be sufficiently accurate in most practical situations (Hämaläinen and Sarvas, 1989); it is also the recommended MEG head model in the Fieldtrip (Oostenveld et al., 2020) and MNE software toolboxes (Hämäläinen, 2010). In this respect, the realistically-shaped three-shell model used in this study already represents a step forward towards a more realistic head modeling, which is expected to improve the accuracy of source reconstruction and connectivity analysis.

Secondly, in-vivo measurements of brain tumor tissue resistivity showed a large variance of resistivity values, even within the same tumor type, as compared to normal tissue (Latikka and Eskola, 2019). Such a variability is conceivably caused by biological variation, such as heterogeneity of tumor cells, presence of edemas, inflammation, necrosis, tumor size, age, etc., and it makes it impossible to assign a single impedance value to a particular pathology (Rajshekhar, 1992) or to give any general model for brain tumor resistivity. To obtain correct resistivity values, individual in-vivo measurements are required (Latikka and Eskola, 2019). In our study, individual measurements of tumor tissue resistivity (or conductivity) were not available; we therefore did not include brain tissue inhomogeneity in head modeling. The main limitation of our study is in the sample size and heterogeneity. Our population allowed us to assess only some aspects of the tumor effect on power and brain connectivity, but not e.g. tumor location or tumor grade. A further limitation of this study is that patient cognitive performance was not assessed during the clinical screening.

Nevertheless, using MEG source-space data and individualized frequency bands, we can conclude that gliomas can widely influence local and long-range brain synchrony, conceivably resulting in alteration in brain function and changes in brain physiology, with a possible role of tumor grade in this process. Differences between our results and previous studies might have arisen due to different inclusion criteria and different selection of the frequency bands. For the future, it seems therefore crucial to perform studies in a larger sample of patients and with standardized protocol and analysis pipeline, which minimize possible confounds (Hari et al., 2018) and enhance confidence in the observed differences. Additionally, cognitive tests would allow us to investigate the relationship between power and connectivity modulations in different frequency bands and impairment in different cognitive domains.

Funding

Funding for this research was provided by the Faculty Resources Grant of the "G. d'Annunzio" University of Chieti-Pescara by Prof. Marzetti.

Declaration of competing interest

The author declared no conflict of interest.

Acknowledgments

The authors would like to thank Gianluca Trevisi, Jyrki Mäkelä and Filippo Zappasodi for useful discussion, and Vincenzo Palatino and all the staff of the MRI facility at the Institute for Advanced Biomedical Technologies (ITAB) for cooperation. This work has been conducted within the framework of the "Departments of Excellence 2018–2022" initiative of the Italian Ministry of Education, University and Research for the Department of Neuroscience, Imaging and Clinical Sciences (DNISC) of the University of Chieti-Pescara.

Appendix A. Supplementary data

Supplementary data to this article can be found online at https://doi.org/10.1016/j.ynirp.2021.100051.

Availability of data and material

The raw data is not publicly available. However, the raw data can be made available by the corresponding author upon request.

Code availability

The Matlab code used for the analyses can be made available by the corresponding author upon request.

Author contributions

FSS, LM, FC, MC and VP designed the study. FSS, FC and MC contributed to the experimental implementation, participant enrollment, evaluation, follow-up, and data collection. FSS and FC contributed to the data analysis and literature search. MR and RN participated in the definition of the regions of interest. FC, VP and LM prepared and finalized the manuscript. All authors have read and approved the manuscript.

References

Alamian, G., Hincapié, A.S., Pascarella, A., Thiery, T., Combrisson, E., Saive, A.L., Martel, V., Althukov, D., Haesebaert, F., Jerbi, K., 2017. Measuring alterations in oscillatory brain networks in schizophrenia with resting-state MEG: state-of-the-art and methodological challenges. Clin. Neurophysiol. 128, 1719–1736. https://doi.org/10.1016/j.clinph.2017.06.246.

Allen, M., Poggiali, D., Whitaker, K., Marshall, T.R., Kievi, R.A., 2019. Raincloud plots: a multi-platform tool for robust data visualization. Wellcome Open Res 4, 63. https://doi.org/10.12688/wellcomeopenres.15191.1.

Baayen, J.C., de Jongh, A., Stam, C.J., de Munck, J.C., Jonkman, J.J., Trenité, D.G., Berendse, H.W., van Walsum, A.M., Heimans, J.J., Puligheddu, M., Castelijns, J.A., Vandertop, W.P., 2003 Winter. Localization of slow wave activity in patients with tumor-associated epilepsy. Brain Topogr. 16 (2), 85–93. https://doi.org/10.1023/b:brat.0000006332.71345.b7.

Bagić, A.I., Funke, M.E., Burgess, R.C., 2020. The wisdom and vision from the ACMEGS inaugural decade. J. Clin. Neurophysiol. 37, 471–482. https://doi.org/10.1097/WNP.0000000000000744.

Baillet, S., 2017. Magnetoencephalography for brain electrophysiology and imaging. Nat. Neurosci. 20, 327–339. https://doi.org/10.1038/nn.4504.

Bandt, S.K., Roland, J.L., Pahwa, M., Hacker, C.D., Bundy, D.T., et al., 2017. The impact of high grade glial neoplasms on human cortical electrophysiology. PloS One 12 (3), e0173448. https://doi.org/10.1371/journal.pone.0173448.

Bartolomei, F., Bosma, I., Klein, M., Baayen, J.C., Reijneveld, J.C., Postma, T.J., et al., 2006a. How do brain tumors alter functional connectivity? A magnetoencephalography study. Ann. Neurol. 59, 128–138. https://doi.org/10.1002/ana.20710.

Bartolomei, F., Bosma, I., Klein, M., Baayen, J.C., Reijneveld, J.C., Postma, T.J., et al., 2006b. Disturbed functional connectivity in brain tumor patients: evaluation by graph analysis of synchronization matrices. Clin. Neurophysiol. 117, 2039–2049. https://doi.org/10.1016/j.clinph.2006.05.018.

Basti, A., Pizzella, V., Chella, F., Romani, G.L., Nolte, G., Marzetti, L., 2018. Disclosing large-scale directed functional connections in MEG with the multivariate phase slope index. Neuroimage 175, 161–175. https://doi.org/10.1016/j.neuroimage.2018.03.004.

Basti, A., Nili, H., Hauk, O., Marzetti, L., Henson, R., 2020. Multi-dimensional connectivity: a conceptual and mathematical review. Neuroimage 117179. https://doi.org/10.1016/j.neuroimage.2020.117179.

Benjamini, Y., Yekutieli, D., 2001. The control of the false discovery rate in multiple testing under dependency. Ann. Stat. 29, 1165–1188.

Borgiotti, G., Kaplan, L.J., 1979. Superresolution of uncorrelated interference sources by using adaptive array technique. IEEE Trans. Antenn. Propag. 27, 842–845. https://doi.org/10.1109/TAP.1979.1142176.

Bosma, I., Stam, C., Douw, L., Bartolomei, F., Heimans, J., Van Dijk, B., et al., 2008a. The influence of low-grade glioma on resting state oscillatory brain activity: a magnetoencephalography study. J. Neuro Oncol. 88, 77–85. https://doi.org/10.1007/s11060-008-9535-3.

Bosma, I., Douw, L., Bartolomei, F., Heimans, J.J., van Dijk, B.W., Postma, T.J., et al., 2008b. Synchronized brain activity and neurocognitive function in patients with low-grade glioma: a magnetoencephalography study. Neuro Oncol. 10, 734–744. https://doi.org/10.1215/15228517-2008-034.

Brookes, M.J., Woolrich, M., Luckhoo, H., Price, D., Hale, J.R., Stephenson, M.C., Barnes, G.R., Smith, S.M., Morris, P.G., 2011. Investigating the electrophysiological basis of resting state networks using magnetoencephalography. Proc. Natl. Acad. Sci. U.S.A. 8, 16783–16788. https://doi.org/10.1073/pnas.1112685108.

Brunetti, M., Marzetti, L., Sepede, G., Zappasodi, F., Pizzella, V., Sarchione, F., Vellante, F., Martinotti, G., Di Giannantonio, M., 2017. Resilience and cross-network connectivity: a neural model for post-trauma survival. Prog. Neuro-Psychopharmacol. Biol. Psychiatry 77, 110–119. https://doi.org/10.1016/j.pnpbp.2017.04.010.

Butz, M., Gross, J., Timmermann, L., Moll, M., Freund, H.-J., Witte, O.W., et al., 2004. Perilesional pathological oscillatory activity in the magnetoencephalogram of patients with cortical brain lesions. Neurosci. Lett. 355, 93–96. https://doi.org/10.1016/j.neulet.2003.10.065.

Chella, F., Zappasodi, F., Marzetti, L., Della Penna, S., Pizzella, V., 2012. Calibration of a multichannel MEG system based on the Signal Space Separation method. Phys. Med. Biol. 57, 4855–4870. https://doi.org/10.1088/0031-9155/57/15/4855.

Chella, F., D'Andrea, A., Basti, A., Pizzella, V., Marzetti, L., 2017. Non-linear analysis of scalp EEG by using bispectra: the effect of the reference choice. Front. Neurosci. 11, 262. https://doi.org/10.3389/fnins.2017.00262.

De Jongh, A., Baayen, J., De Munck, J., Heethaar, R., Vandertop, W., Stam, C., 2003. The influence of brain tumor treatment on pathological delta activity in MEG. Neuroimage 20, 2291. https://doi.org/10.1016/j.neuroimage.2003.07.030.

de Pasquale, F., Della Penna, S., Snyder, A.Z., Marzetti, L., Pizzella, V., Romani, G.L., Corbetta, M., 2012. A cortical core for dynamic integration of functional networks in the resting human brain. Neuron 74, 753–764. https://doi.org/10.1016/j.neuron.2012.03.031.

Donoghue, T., Schaworonkow, N., Voytek, B., 2021. Methodological considerations for studying neural Oscillations. Eur. J. Neurosci. 1–26. https://doi.org/10.1111/ejn.15361.

Engel, A.K., Gerloff, C., Hilgetag, C.C., Nolte, G., 2013. Intrinsic coupling modes: multiscale interactions in ongoing brain activity. Neuron 80, 867–886. https://doi.org/10.1016/j.neuron.2013.09.038.

Fonov, V.S., Evans, A.C., McKinstry, R.C., Almli, C.R., Collins, D.L., 2009. Unbiased nonlinear average age-appropriate brain templates from birth to adulthood. Neuroimage 47 (Suppl. 1), 1053–8119. https://doi.org/10.1016/S1053-8119(09)70884-5. S102ISSN.

Fonov, V.S., Evans, A.C., Botteron, K., Almli, C.R., McKinstry, R.C., Collins, D.L., 2011. Unbiased average age-appropriate atlases for pediatric studies. Neuroimage 54, 313–327. https://doi.org/10.1016/j.neuroimage.2010.07.033.

Fries, P., 2005. A mechanism for cognitive dynamics: neuronal communication through neuronal coherence. Trends Cognit. Sci. 90, 474–480. https://doi.org/10.1016/j.tics.2005.08.011.

Gloor, R., Kalabay, O., Giard, N., 1968. The electroencephalogram in diffuse encephalopathies. Electroencephalographic correlates of gray and white matter lesions. Brain 91, 779–802. https://doi.org/10.1093/brain/91.4.779.

Goldensohn, E.S., 1979. Use of EEG for evaluation of focal intracranial lesions. In: Klass, D.W., Daly, D.D. (Eds.), Current Practice of Clinical Electro-Encephalography. Raven, New York, pp. 307–341.

Gómez, C., Stam, C.J., Hornero, R., Fernández, A., Maestú, F., 2009. Disturbed beta band functional connectivity in patients with mild cognitive impairment: an MEG study. IEEE Trans. Biomed. Eng. 56, 1683–1690.

Good, P., 1994. Permutation Tests: a Practical Guide to Resampling Methods for Testing Hypotheses. Springer-Verlag, New York.

Gramfort, A., Papadopoulo, T., Olivi, E., Clerc, M., 2010. OpenMEEG: opensource software for quasistatic bioelectromagnetics. Biomed. Eng. Online 6, 9–45. https://doi.org/10.1186/1475-925X-9-45.

Greicius, M., 2008. Resting-state functional connectivity in neuropsychiatric disorders. Curr. Opin. Neurol. 21, 424–430. https://doi.org/10.1097/WCO.0b013e328306f2c5.

Gross, J., Baillet, S., Barnes, G., Henson, R., Hillebrand, A., 2013. Good practice for conducting and reporting MEG research. Neuroimage 65, 349–363. https://doi.org/10.1016/j.neuroimage.2012.10.001.

Guggisberg, A.G., Honma, S.M., Findlay, A.M., Dalal, S.S., Kirsch, H.E., Berger, M.S., et al., 2008. Mapping functional connectivity in patients with brain lesions. Ann. Neurol. 63, 193–203. https://doi.org/10.1002/ana.21224.

Haegens, S., Cousijn, H., Wallis, G., Harrison, P.J., Nobre, A.C., 2014. Inter- and intra-individual variability in alpha peak frequency. Neuroimage 92, 46–55. https://doi.org/10.1016/j.neuroimage.2014.01.049.

Hämäläinen, M.S., 2010. MNE Software User's Guide. https://mne.tools/mne-c-manual/MNE-manual-2.7.3.pdf. (Accessed 1 June 2021).

Hämaläinen, M.S., Sarvas, J., 1989. Realistic conductivity geometry model of the human head for interpretation of neuromagnetic data. IEEE Trans. Biomed. Eng. 36, 165–171. https://doi.org/10.1109/10.16463.

Hämäläinen, M.S., Hari, R., Ilmoniemi, R.J., Knuutila, J., Lounasmaa, O.V., 1993. Magnetoencephalography—theory, instrumentation, and applications to noninvasive studies of the working human brain. Rev. Mod. Phys. 65, 413. https://doi.org/10.1103/RevModPhys.65.413.

Hari, R., Baillet, S., Barnes, G., Burgess, R., Forss, N., Gross, J., Hämäläinen, M., Jensen, O., Kakigi, R., Mauguière, F., Nakasato, N., Puce, A., Romani, G.L., Schnitzler, A., Taulu, S., 2018. IFCN-endorsed practical guidelines for clinical magnetoencephalography (MEG). Clin. Neurophysiol. 129, 1720–1747. https://doi.org/10.1016/j.clinph.2018.03.042.

Hillebrand, A, Barnes, GR, Bosboom, JL, Berendse, HW, Stam, CJ, 2012. Frequency-dependent functional connectivity within resting-state networks: an atlas-based MEG beamformer solution. Neuroimage 59, 3909.

Hintze, J.L., Nelson, R.D., 1998. Violin plots: a box plot-density trace synergism. Am Stat 52 (2), 181–184. https://doi.org/10.1080/00031305.1998.10480559.

Hyvärinen, A., Oja, E., 2000. Independent component analysis: algorithms and applications. Neural Network. 13, 411–430.

Klein, M., Taphoorn, M.J., Heimans, J.J., et al., 2001. Neurobehavioral status and health-related quality of life in newly diagnosed high-grade glioma patients. J. Clin. Oncol. 19 (20), 4037–4047. https://doi.org/10.1200/JCO.2001.19.20.4037.

Klein, M., Postma, T.J., Taphoorn, M.J., et al., 2003. The prognostic value of cognitive functioning in the survival of patients with high-grade glioma. Neurology 61 (12), 1796–1798. https://doi.org/10.1212/01.wnl.0000098892.33018.4c, 14.

Klimesch, W., 1999. EEG alpha and theta oscillations reflect cognitive and memory performance: a review and analysis. Brain Res. Rev. 29 (2–3), 169–195. https://doi.org/10.1016/S0165-0173(98)00056-3.

Larson-Prior, L.J., Oostenveld, R., Della Penna, S., Michalareas, G., Prior, F., Babajani-Feremi, A., Schoffelen, J.-M., Marzetti, L., de Pasquale, F., Di Pompeo, F., Stout, J., Woolrich, M., Luo, Q., Bucholz, R., Fries, P., Pizzella, V., Romani, G.L., Corbetta, M., Snyder, A.Z., 2013. Adding dynamics to the human connectome Project with MEG. Neuroimage 80, 190–201. https://doi.org/10.1016/j.neuroimage.2013.05.056.

Latikka, J., Eskola, H., 2019. The resistivity of human brain tumours in vivo. Ann. Biomed. Eng. 47, 706–713. https://doi.org/10.1007/s10439-018-02189-7.

Lee, A.T., Faltermeier, C., Morshed, R.A., Young, J.S., Kakaizada, S., Valdivia, C., Findlay, A.M., Tarapore, P.E., Nagarajan, S.S., Hervey-Jumper, S.L., Berger, M.S., 2020. The impact of high functional connectivity network hub resection on language task performance in adult low- and high-grade glioma. J. Neurosurg. 134 (4), 1102–1112. https://doi.org/10.3171/2020.1.JNS192267.

Lizarazu, M., Gil-Robles, S., Pomposo, I., Nara, S., Amoruso, L., Quiñones, I., Carreiras, M., 2020. Spatiotemporal dynamics of postoperative functional plasticity in patients with brain tumors in language areas. Brain Lang. 202, 104741. https://doi.org/10.1016/j.bandl.2019.104741.

Martino, J., Honma, S.M., Findlay, A.M., Guggisberg, A.G., Owen, J.P., Kirsch, H.E., et al., 2011. Resting functional connectivity in patients with brain tumors in eloquent areas. Ann. Neurol. 69, 521–532. https://doi.org/10.1002/ana.22167.

Ewald, A., Marzetti, L., Zappasodi, F., Meinecke, F., Nolte, G., 2011. Estimating true brain connectivity from EEG/MEG data invariant to linear and static transformations in sensor space. Neuroimage 60, 476–488. https://doi.org/10.1016/j.neuroimage.2011.11.084.

Marzetti, L., Della Penna, S., Snyder, A., Pizzella, V., Nolte, G., de Pasquale, F., et al., 2013. Frequency specific interactions of MEG resting state activity within and across brain networks as revealed by the multivariate interaction measure. Neuroimage 79, 172–183. https://doi.org/10.1016/j.neuroimage.2013.04.062.

Marzetti, L., Basti, A., Chella, F., D'Andrea, A., Syrjälä, J., Pizzella, V., 2019. Brain functional connectivity through phase coupling of neuronal oscillations: a perspective from magnetoencephalography. Front. Neurosci. 13, 964. https://doi.org/10.3389/fnins.2019.00964.

Mosher, J.C., Leahy, R.M., Lewis, P.S., 1999. EEG and MEG: forward solutions for inverse methods. IEEE Trans. Biomed. Eng. 46, 245–259. https://doi.org/10.1109/10.748978.

Niedermeyer, E., Lopes da Silva, F., 2005. Electroencephalography: basic principles, clinical applications, and related fields. Lippincott Williams and Wilkins), Philadelphia, PA.

Nolte, G., Bai, O., Wheaton, L., Mari, Z., Vorbach, S., Hallett, M., 2004. Identifying true brain interaction from EEG data using the imaginary part of coherency. Clin. Neurophysiol. 115, 2292–2307. https://doi.org/10.1016/j.clinph.2004.04.029.

Oostenveld, R., Fries, P., Maris, E., Schoffelen, J.-M., 2011. FieldTrip: open source software for advanced analysis of MEG, EEG, and invasive electrophysiological data. Comput. Intell. Neurosci. 156869. https://doi.org/10.1155/2011/156869, 2011.

Oostenveld, R., Schoffelen, J.-M., Spaak, E., 2020. Creating a volume conduction model of the head for source-reconstruction of MEG data. https://www.fieldtriptoolbox.org/tutorial/headmodel_meg/. (Accessed 1 June 2021).

Oshino, S., Kato, A., Wakayama, A., Taniguchi, M., Hirata, M., Yoshimine, T., 2007. Magnetoencephalographic analysis of cortical oscillatory activity in patients with brain tumors: synthetic aperture magnetography (SAM) functional imaging of delta band activity. Neuroimage 34, 957–964. https://doi.org/10.1016/j.neuroimage.2006.08.054.

Percival, D.B., Walden, A.T., 1993. Spectral Analysis for Physical Applications: Multitaper and Conventional Univariate Techniques. Cambridge University Press, Cambridge.

Pizzella, V., Della Penna, S., Del Gratta, C., Romani, G.L., 2001. SQUID systems for biomagnetic imaging. Supercond. Sci. Technol. 14, R79–R114. https://doi.org/10.1088/0953-2048/14/7/201.

Pizzella, V., Marzetti, L., Della Penna, S., de Pasquale, F., Zappasodi, F., Romani, G.L., 2014. Magnetoencephalography in the study of brain dynamics. Funct. Neurol. 29, 241–253.

Rajshekhar, V., 1992. Continuous impedance monitoring during CT-guided stereotactic surgery: relative value in cystic and solid lesions. Br. J. Neurosurg. 6, 439–444.

Reijneveld, J.C., Sitskoorn, M.M., Klein, M., Nuyen, J., Taphoorn, M.J., 2001. Cognitive status and quality of life in patients with suspected versus proven low-grade gliomas. Neurology 56 (5), 618–623. https://doi.org/10.1212/wnl.56.5.618.

Ricci, L., Assenza, G., Pulitano, P., Simonelli, V., Vollero, L., Lanzone, J., Mecarelli, O., Di Lazzaro, V., Tombini, M., 2021. Measuring the effects of first antiepileptic medication in Temporal Lobe Epilepsy: predictive value of quantitative-EEG analysis. Clin. Neurophysiol. 132 (1), 25–35. https://doi.org/10.1016/j.clinph.2020.10.020.

Schnitzler, A., Gross, J., 2005. Normal and pathological oscillatory communication in the brain. Nat. Rev. Neurosci. 285–296. https://doi.org/10.1038/nrn1650.

Seghier, M.L., 2008. Laterality index in functional MRI: methodological issues. Magn. Reson. Imag. 26 (5), 594–601. https://doi.org/10.1016/j.mri.2007.10.010.

Sekihara, K., Nagarajan, S.S., 2008. Adaptive spatial filters for electromagnetic brain imaging. In: In: Series in Biomedical Engineering. Springer-Verlag, Berlin Heidelberg. https://doi.org/10.1007/978-3-540-79370-0.

Sekihara, K., Nagarajan, S.S., Poeppel, D., Marantz, A., Miyashita, Y., 2001. Reconstructing spatio-temporal activities of neural sources using an MEG vector beamformer technique. IEEE (Inst. Electr. Electron. Eng.) Trans. Biomed. Eng. 48 (7), 760–771. https://doi.org/10.1109/10.930901.

Stam, C., Jones, B., Manshanden, I., Cappellen, M., Montez, T., Verbunt, J., et al., 2006. Magnetoencephalographic evaluation of resting-state functional connectivity in Alzheimer's disease. Neuroimage 32, 1335–1344. https://doi.org/10.1016/j.neuroimage.2006.05.033.

Stenroos, M., Hunold, A., Haueisen, J., 2014. Comparison of three-shell and simplified volume conductor models in magnetoencephalography. Neuroimage 94, 337–348. https://doi.org/10.1016/j.neuroimage.2014.01.006. PMID: 24434678.

Taphoorn, M.J., Klein, M., 2004. Cognitive deficits in adult patients with brain tumours. Lancet Neurol. 3 (3), 159–168. https://doi.org/10.1016/0360-3016(94)90423-5.

Taphoorn, M.J., Heimans, J.J., Snoek, F.J., Lindeboom, J., Karim, A.B., 1994. Quality of life and neuropsychological functions in long-term low-grade glioma survivors. Int. J. Radiat. Oncol. Biol. Phys. 29 (5), 1201–1202, 20.

Tarapore, P.E., Martino, J., Guggisberg, A.G., Owen, J., Honma, S.M., Findlay, A., et al., 2012. Magnetoencephalographic imaging of resting-state functional connectivity predicts postsurgical neurological outcome in brain gliomas. Neurosurgery 71, 1012–1022. https://doi.org/10.1227/NEU.0b013e31826d2b78.

Tzourio-Mazoyer, N., Landeau, B., Papathanassiou, D., Crivello, F., Etard, O., Delcroix, N., Mazoyer, B., Joliot, M., 2002. Automated anatomical labeling of activations in SPM using a macroscopic anatomical parcellation of the MNI MRI single-subject brain. Neuroimage 15 (1), 273–289. https://doi.org/10.1006/nimg.2001.0978.

van Dellen, E., de Witt Hamer, P.C., Douw, L., Klein, M., Heimans, J.J., Stam, C.J., Reijneveld, J.C., Hillebrand, A., 2013. Connectivity in MEG resting-state networks increases after resective surgery for low-grade glioma and correlates with improved cognitive performance. Neuroimage: Clinical 2, 1–7. https://doi.org/10.1016/j.nicl.2012.10.007.

Van Veen, B.D., Drongelen, W., Yuchtman, M., Suzuki, A., 1997. Localization of brain electrical activity via linearly constrained minimum variance spatial filtering. IEEE Trans. Biomed. Eng. 44, 867–880. https://doi.org/10.1109/10.623056.

van Wijk, B.C., Willemse, R.B., Vandertop, W.P., Daffertshofer, A., 2012. Slowing of M1 oscillations in brain tumor patients in resting state and during movement. Clin. Neurophysiol. 123, 2212–2219. https://doi.org/10.1016/j.clinph.2012.04.012.

Vieth, J.B., Kober, H., Grummich, P., 1996. Sources of spontaneous slow waves associated with brain lesions, localized by using the MEG. Brain Topogr. 8, 215–221. https://doi.org/10.1007/BF01184772.

Wang, H.S., Busse, E.W., 1969. EEG of healthy old persons—a longitudinal study. I. Dominant background activity and occipital rhythm. J. Gerontol. 24 (4), 419–426. https://doi.org/10.1093/geronj/24.4.419.

Yushkevich, P., Gao, Y., Gerig, G., 2016. ITK-SNAP: an interactive tool for semi-automatic segmentation of multi-modality biomedical images. Conf Proc IEEE Eng Med Biol Soc 3342–3345. https://doi.org/10.1109/EMBC.2016.7591443, 2016.